J. Fluid Mech. (1993), *vol.* 248, *pp.* 403–423

A model of defect-induced pairing in mixing layers

By RUIXIN YANG†, FREDERIC K. BROWAND, PIERRE COULLET‡ AND PATRICK HUERRE‖

Department of Aerospace Engineering, University of Southern California, Los Angeles, CA 90089-1191, USA

(Received 10 September 1991 and in revised form 22 September 1992)

Experiments have shown that the well-known vortex pairing process may take place first in defect regions where the fundamental structure is weakest. A model is introduced here to describe this defect-induced pairing process. The model is constructed in such a way that, in a certain parameter range, a stable fundamental mode and a stable subharmonic mode may coexist. The numerical simulation demonstrates that, when initial conditions consist of a dominant fundamental with one or more defects, the subharmonic component is preferentially generated in the cores of these defects. Moreover, the results also indicate that pairing may first commence wherever the fundamental mode is weakest provided the white-noise level of the subharmonic is high enough. The numerical results are in good agreement with experimental observations.

1. Introduction

In the evolution of mixing layers, the interactions between large-scale vortex structures play an important role. During a pairing event, two neighbouring vortices merge to form a single larger vortex, having a wavelength double that of the original two. Thus successive pairings of neighbouring vortices govern in a primary way the streamwise growth process, as demonstrated by Winant & Browand (1974), Brown & Roshko (1974) and Ho & Huang (1982) among others. For a review of the dynamics of coherent structures in mixing layers, the reader is referred to Ho & Huerre (1984).

Experiments have shown that the large-scale vortices in mixing layers are not perfectly two-dimensional but only quasi-two-dimensional (Browand & Troutt 1980, 1985; Browand & Prost-Domasky 1990). One such experimental result is illustrated in figure 1. A sequence of vortices is visualized by a two-level contour map of the longitudinal component of fluctuation velocity obtained from a multiprobe hot-wire rake situated several wavelengths downstream from the origin of the flow. In this case the darkened portions of the image correspond to velocities above the mean value (positive). The observed velocity field is consistent with vortices which are nearly parallel to the span (horizontal), but contain branching interconnections, as at A. Because of their similarity to dislocations in crystals, they are sometimes

† Present address: Institute for Computational Sciences & Informatics, George Mason University, Fairfax, VA 22030-4444, USA.

‡ Permanent address: Institut Nonlinéaire de Nice, Université de Nice, Parc Valrose, 06108 Nice, France.

‖ Present address: Laboratoire d'hydrodynamique (LADHYX), Ecole Polytechnique. 91128 Palaiseau Cedex, France.

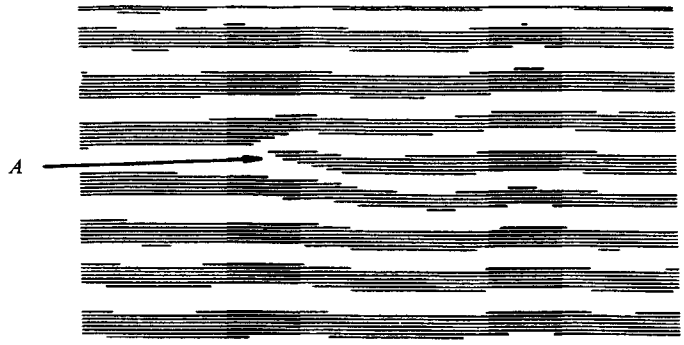

FIGURE 1. Example of an experimentally generated defect in the mixing layer. Horizontal axis is spanwise position, vertical axis is time. Darkened regions represent positive streamwise fluctuations, the blank regions represent negative streamwise fluctuation velocity.

referred to as dislocation defects or simply dislocations. They occur as at A or with opposite polarity (reverse the dark and light regions) with equal frequency. Such dislocations occur naturally and spontaneously in the flow, and are the most prominent pattern irregularities arising in the developing flow field. It is natural to ask what role they play in the further development of the mixing layer.

A dislocation defect describes a point where the phase description of a field is singular. For instance, if v is the perturbed velocity in a mixing layer, we can write

$$v = A(x,z,t)\,\mathrm{e}^{\mathrm{i}\theta(x,z,t)}\,\mathrm{e}^{\mathrm{i}\alpha x} + \text{c.c.},$$

where α is the fundamental pattern wavenumber, $A(x,z,t)$ its real positive amplitude, and $\theta(x,z,t)$ the residual phase. Around a simple dislocation defect as in figure 1, the value of the residual phase has a 2π jump. At the cores of a dislocation, the phase singularity requires the field strength $A(x,z,t)$ to be zero. It is not known what the vorticity field looks like in the immediate vicinity of such a defect. For our purpose, it is only necessary to identify such defects as regions of diminished pattern strength, as illustrated in figure 2. The defect in figure 2 was produced with a small acoustic perturbation to establish a phase reference and allow velocity measurements on a much finer grid.

The nucleation and expansion of one stable state into a more complex metastable state containing defects have been investigated by Coullet, Gil & Repaux (1989). These authors use Ginzburg–Landau-type models as basic equations to describe the process and they exploit known results concerning the properties of fronts and defects in potential systems as described for instance in Balian, Klemann & Poirier (1981) and Lifshits & Pitaevskii (1981). For the particular one-dimensional model

$$\frac{\partial A}{\partial t} = \mu A + A^3 - A^5 + \frac{\partial^2 A}{\partial x^2},$$

considered by Coullet *et al.* (1989), three uniform stable states A_+, A_- and A_0 are possible in a certain range of control parameter μ. The relative stability of the solutions can be compared by calculating the corresponding values of a potential functional F from which the model equation is derived. Solutions A_+ and A_- have the same absolute values but opposite sign. The corresponding values of the functional are the same, and so are their stabilities. Therefore, when $F(A_\pm) < F(A_0)$, A_0 is only metastable and the other two states A_+ and A_- are stable. When $F(A_\pm) > F(A_0)$, the

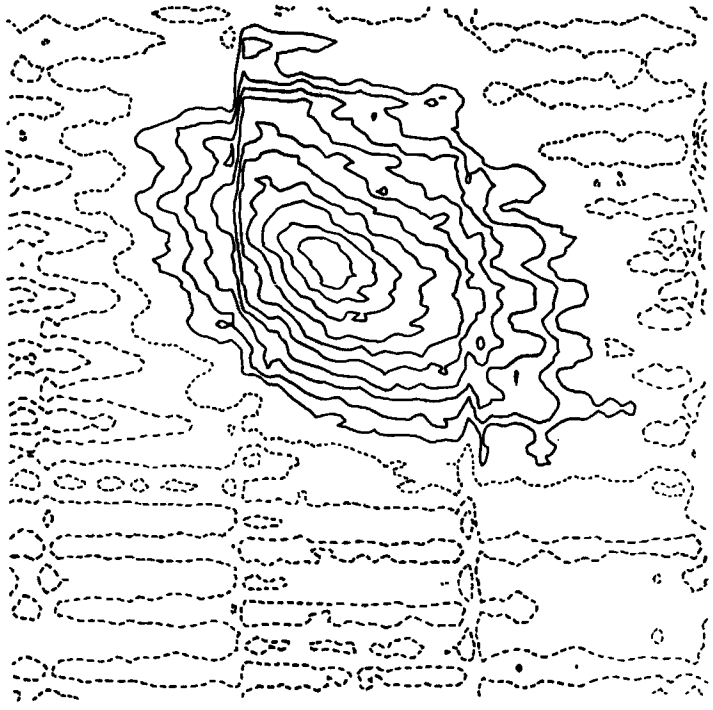

FIGURE 2. An example of a dislocation defect observed in the mixing layer. Horizontal axis is span, vertical axis is time. Contours are level value of velocity fluctuation modulus. The mixing layer is weakly forced to produce the defect. The values of the modulus associated with closed solid lines decrease inwards.

stabilities are reversed. The symmetry between A_+ and A_- allows the solution that connects them to be stationary. The solutions connecting A_+ and A_- are referred to as defects because of the 2π phase jump associated with their opposite signs. The solutions connecting A_0 and A_+ (or A_-) are not symmetrical, and they move with a finite velocity. The direction of motion depends on the relative stabilities of A_+ and A_0 and always leads to the expansion of the stable state. When A_0 is stable and A_+ (and A_-) is metastable, a state consisting of A_+, A_- and the defect connecting them will generate the A_0 state in the core of the defect. The defect is then replaced by two fronts – the solution connecting A_0 and A_+, and the solution connecting A_0 and A_-. The motion of the fronts will result in the expansion of the stable A_0 state at a cost to the A_+ and A_- states.

The pairing process observed in experiments is qualitatively similar to the phenomenon described by Coullet *et al.* From an energetics point of view, one might argue that the pairing process in mixing layers is a competition between the energy associated with the vortices of wavenumber α and the energy associated with those of the subharmonic wavenumber $\frac{1}{2}\alpha$, with the subharmonic mode being dominant. In the present investigation we propose a phenomenological model to describe this energy exchange and in particular pairing events induced by defects of the fundamental. Rather than conducting an in-depth asymptotic analysis starting from the basic equations of motion, we postulate an amplitude evolution model that is consistent with the symmetry properties of the physical problem and with known linear and weakly nonlinear stability characteristics of mixing layers. It is not

claimed that the model presented here is unique but only that it contains the minimal structure necessary to account for the observed phenomena. This strategy has proven to be successful in pattern-formation studies in closed flows, for instance in describing nonlinear travelling wave states in binary fluid convection (Cross 1988). It has also been pertinent in qualitative descriptions of the onset of Kármán vortex sheets behind circular cylinders (Chomaz, Huerre & Redekopp 1988). In the following sections, we will present the model equations, discuss the local bifurcation structure, and analyse the results of numerical simulations to compare them with experimental observations.

2. The subharmonic interaction model

2.1. *Evolution equations*

An amplitude evolution model is proposed to describe the interactions between the fundamental and the subharmonic component. The streamwise, cross-stream and spanwise coordinates in the flows are denoted by x, y and z respectively. The assumption is made that the properties in the cross-stream direction y can be well represented by their values in a horizontal plane or by their averages in y. Therefore, the model is spatially two-dimensional, and it is described in space spanned by z and x. The equations are

$$\frac{\partial A_1}{\partial t} = \mu_1 A_1 - [a_1|A_1|^2 + b_1|A_2|^2]A_1 + \gamma_1 \frac{\partial^2 A_1}{\partial x^2} + \gamma_2 \frac{\partial^2 A_1}{\partial z^2}, \tag{1}$$

$$\frac{\partial A_2}{\partial t} = \mu_2 A_2 - [a_2|A_2|^2 + b_2|A_1|^2]A_2 + \delta_1 \frac{\partial^2 A_2}{\partial x^2} + \delta_2 \frac{\partial^2 A_2}{\partial z^2}, \tag{2}$$

where the complex functions A_1 and A_2 represent the amplitudes of the subharmonic mode and the fundamental mode respectively. All the coefficients in the equations are assumed to be real; μ_1 and μ_2 are the control parameters; a_1 and a_2 are the Landau constants pertaining to each mode; b_1 and b_2 describe the coupling between A_1 and A_2; and γ_1, γ_2, δ_1, and δ_2 are diffusion coefficients.

The above model cannot be rigorously derived by performing a multiple-scale analysis close to onset, as in classical weakly nonlinear studies. It can, however, be partially justified by appealing to symmetry considerations, to the known characteristics of linear instability waves in mixing layers, and to available results from previous weakly nonlinear investigations. First we note that (1) and (2) respect the symmetry properties of the mixing layers being modelled, namely invariance under time translation, space translations along x and z, and space reflections with respect to x and z. Furthermore, from the linear temporal stability properties of antisymmetric mixing layers (Michalke 1964) it is known that the dispersion relation between the frequency ω and the wavenumber α is necessarily of the form $\omega = i\omega_i(\alpha)$, where ω_i is real. This implies that the coefficients of all linear terms in (1) and (2) necessarily have to be real. Finally, it is known from previous multiple-scale analyses (Churilov & Shukhman 1987; Huerre 1987) that the nonlinear evolution of weakly amplified waves in mixing layers close to the cutoff wavenumber gives rise to a nonlinear self-interaction term $|A_2|^2A_2$ with a real and positive Landau constant a_2. We shall assume that the subharmonic A_1 is subjected to a similar nonlinear saturation term $|A_1|^2A_1$ with $a_1 > 0$. The cubic terms $|A_1|^2A_2$ and $|A_2|^2A_1$ have been included to account for energy exchanges between the two modes.

The fact that the interacting wavenumbers differ from each other by a factor of two might lead one to suspect that the model should also contain quadratic nonlinearities of the form $A_2 A_1^*$ in (1) and A_1^2 in (2). Such terms should indeed be included when subharmonic resonance takes place, i.e. when the interacting disturbances have wavenumbers in the ratio 1:2 *and* propagate at the same phase speed. This mechanism has been examined in detail by Kelly (1967, 1968) and Monkewitz (1988) to account for the emergence of the subharmonic component in homogeneous or stratified mixing layers. As noted in Ho & Huerre (1984) subharmonic resonance modes with quadratic nonlinearities are not necessarily pertinent in the present context since the required resonance conditions are not satisfied: the subharmonic growth rate is order unity. We have therefore chosen to limit the study to cubic interaction terms only. This restriction preserves the variational nature of the model and greatly simplifies the interpretation of the result in terms of stable and metastable states.

In order to understand the meaning of the fields A_1 and A_2 more clearly, we can write down a physical dependent variable, say the perturbed velocity v, as $v = \mathrm{Re}\,(\psi)$ where

$$\psi = -\mathrm{i}[A_1(x,z,t)\,\mathrm{e}^{\mathrm{i}\alpha x/2} + A_2(x,z,t)\,\mathrm{e}^{\mathrm{i}\alpha x}] \tag{3}$$

is associated with the strength of the vortices in the mixing layer. When $|A_2|$ is much larger than $|A_1|$, the vortices at the fundamental wavenumber α dominate. Conversely, the subharmonic mode of wavenumber $\frac{1}{2}\alpha$ overwhelms the field when $|A_1|$ is much larger than $|A_2|$.

Equations (1) and (2) derive from a Lyapunov functional, and can be written in the form

$$\frac{\partial A_1}{\partial t} = -\frac{1}{b_2}\frac{\delta F}{\delta A_1^*}, \tag{4}$$

$$\frac{\partial A_2}{\partial t} = -\frac{1}{b_1}\frac{\delta F}{\delta A_2^*}, \tag{5}$$

with

$$F = \int \rho\left(A_1, \frac{\partial A_1}{\partial x}, \frac{\partial A_1}{\partial z}, A_2, \frac{\partial A_2}{\partial x}, \frac{\partial A_2}{\partial z}\right) \mathrm{d}x\,\mathrm{d}z. \tag{6}$$

The asterisks denote complex conjugates and the Lyapunov functional density ρ is defined as

$$\rho\left(A_1, \frac{\partial A_1}{\partial x}, \frac{\partial A_1}{\partial z}, A_2, \frac{\partial A_2}{\partial x}, \frac{\partial A_2}{\partial z}\right) = b_2\left[-\mu_1 |A_1|^2 + \frac{a_1 |A_1|^4}{2} + \gamma_1 \left|\frac{\partial A_1}{\partial x}\right|^2 + \gamma_2 \left|\frac{\partial A_1}{\partial z}\right|^2\right]$$
$$+ b_1\left[-\mu_2 |A_2|^2 + \frac{a_2 |A_2|^4}{2} + \delta_1 \left|\frac{\partial A_2}{\partial x}\right|^2 + \delta_2 \left|\frac{\partial A_2}{\partial z}\right|^2\right] + b_1 b_2 |A_1|^2 |A_2|^2. \tag{7}$$

The local bifurcation analysis is carried out for the spatially homogeneous form of (1) and (2), that is *without the diffusion terms*. Under the condition

$$a_1 a_2 - b_1 b_2 < 0, \tag{8}$$

the bifurcation diagram is sketched in figure 3. The stationary solutions are shown with μ_2 fixed and μ_1 as the varying control parameter. The solid lines represent the stable states and the dashed lines indicate the unstable states. The corresponding phase portraits for some typical μ_1 values are given in figure 4. Figure 4 (*a*) illustrates

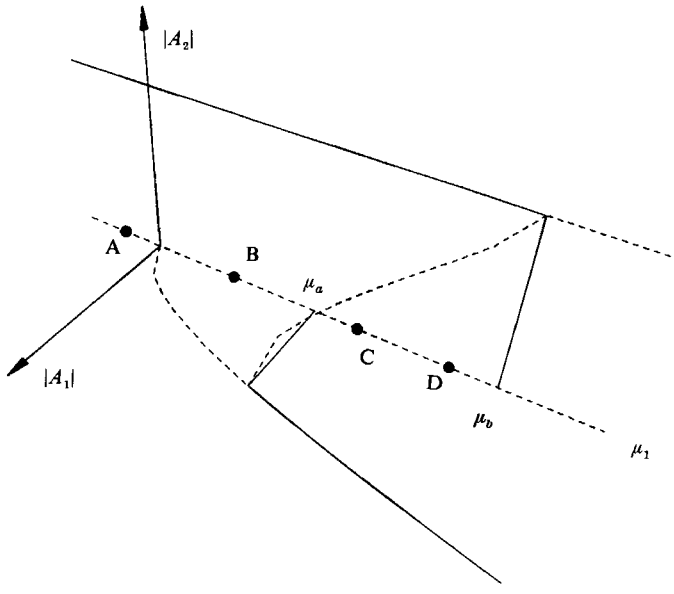

FIGURE 3. Local bifurcation diagram for the model under the condition $a_1 a_2 - b_1 b_2 < 0$. ($\mu_a = (a_1/b_2)\mu_2, \mu_b = (b_1/a_2)\mu_2$). Solid lines represent stable states and the dashed lines unstable states.

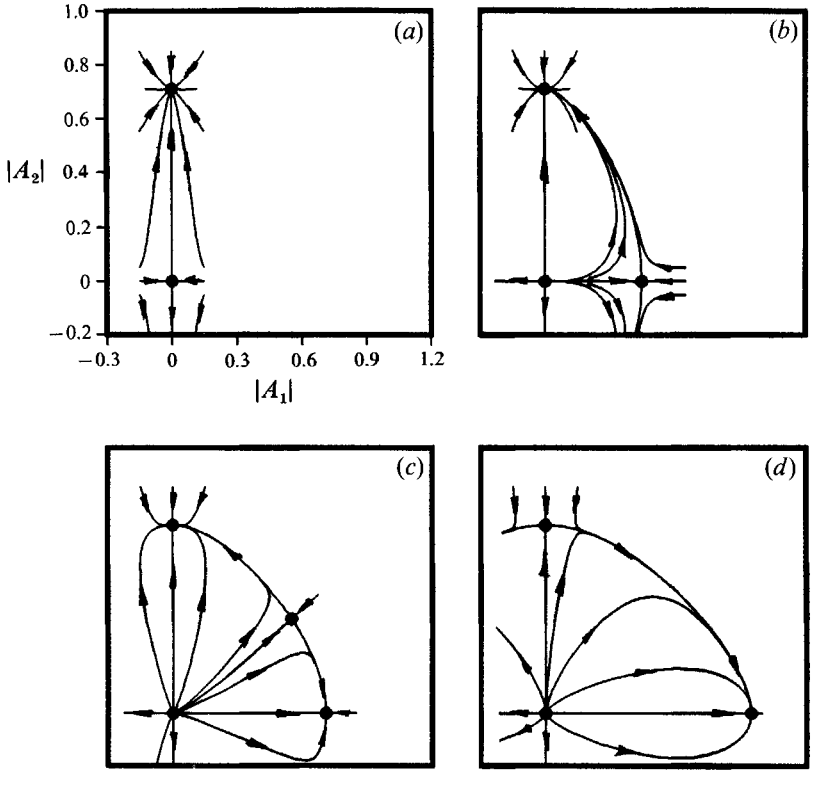

FIGURE 4. Phase portraits of stationary solutions under the condition $a_1 a_2 - b_1 b_2 < 0$ ($a_1 = 1.0$, $a_2 = 1.2, b_1 = 1.6, b_2 = 1.5; \mu_2 = 0.6, \mu_a = 0.4, \mu_b = 0.8$). (*a*) $\mu_1 < 0$ ($\mu_1 = -0.1$); (*b*) $0 < \mu_1 < \mu_a$ ($\mu_1 = 0.2$); (*c*) $\mu_a < \mu_1 < \mu_b$ ($\mu_1 = 0.5$); (*d*) $\mu_1 > \mu_b$ ($\mu_1 = 0.9$).

the case $\mu_1 < 0$ where there are two stationary solutions, one being stable and the other unstable. The phase portrait in the range $0 < \mu_1 < \mu_a (\mu_a = (a_1/b_2)\mu_2)$ is given in figure 4(*b*) where the number of stationary states increases to three with one being stable and the other two unstable. There are four stationary solutions when $\mu_a < \mu_1 < \mu_b (\mu_b = (b_1/a_2)\mu_2)$ as shown in figure 4(*c*), two of them being stable and the others unstable. Figure 4(*d*) represents a typical phase portrait for the case $\mu_1 > \mu_b$. The overall structure looks similar to the case $0 < \mu_1 < \mu_a$, figure 4(*b*), but the two non-zero stationary solutions have exchanged their stabilities.

The most interesting region is $\mu_a < \mu_1 < \mu_b$ where two stable stationary states coexist. The two stable solutions, $A_1 = 0$; $|A_2| = (\mu_2/a_2)^{\frac{1}{2}}$ and $|A_1| = (\mu_1/a_1)^{\frac{1}{2}}$; $A_2 = 0$, represent the fundamental component and the subharmonic component respectively. In terms of the Lyapunov functional, there are two local minima corresponding to the two solutions. Their relative stabilities can be determined by comparing the values of the Lyapunov functional for each. Since both the fundamental state and the subharmonic state are homogeneous, the comparison of the Lyapunov functional values can be made by considering the density ρ only. The value of ρ at the fundamental state ($A_1 = 0$; $|A_2| = (\mu_2/a_2)^{\frac{1}{2}}$) is

$$\rho(F) = -b_1 \mu_2^2/(2a_2), \tag{9}$$

and the corresponding value for the subharmonic state ($|A_1| = (\mu_1/a_1)^{\frac{1}{2}}$; $A_2 = 0$) is

$$\rho(S) = -b_2 \mu_1^2/(2a_1). \tag{10}$$

One can obtain a critical value of the control parameter where $\rho(F) = \rho(S)$, which gives

$$\mu_c = \left(\frac{a_1 b_1}{a_2 b_2}\right)^{\frac{1}{2}} \mu_2. \tag{11}$$

When $\mu_1 < \mu_c, \rho(F) < \rho(S)$, the fundamental solution is stable and the subharmonic solution is metastable. On the other hand, when $\mu_1 > \mu_c, \rho(F) > \rho(S)$, the situation is reversed. During a time evolution with both F and S present, the two states will compete with one other. When the fundamental solution is stable ($\mu_1 < \mu_c$), the final state will likely be a pattern of fundamental wavenumber α. On the other hand, the pattern of subharmonic wavenumber $\frac{1}{2}\alpha$ should eventually dominate the field when $\mu_1 > \mu_c$.

2.2. *Model limitations*

The model has been required to possess the invariances and symmetries which underlie the physical circumstance. The equations have not been derived as a rational approximation (limit-process expansion) of the Navier–Stokes equations. While such an association would be most welcome, it seems beyond the range of possibility at present. It will be shown that some of the numerical coefficients can be chosen by tuning the model equations with the help of experimental observations. Several aspects of the correspondence between model and experiment must therefore be examined.

The equations describe the temporal evolution of a perturbation field satisfying periodic boundary conditions in both space dimensions. They are most directly applicable to temporally evolving mixing layers. The experimental flow one wishes to represent develops spatially in a downstream (flow) direction. The connection can be made by supposing the flow to evolve in a coordinate system fixed to the large structure which is convecting down-stream at average speed between the two streams $\bar{U}$. That is, x and t are connected in the experiment and model by the relation $x = \bar{U}t$. This transformation is not exact, but it is an often used approximation.

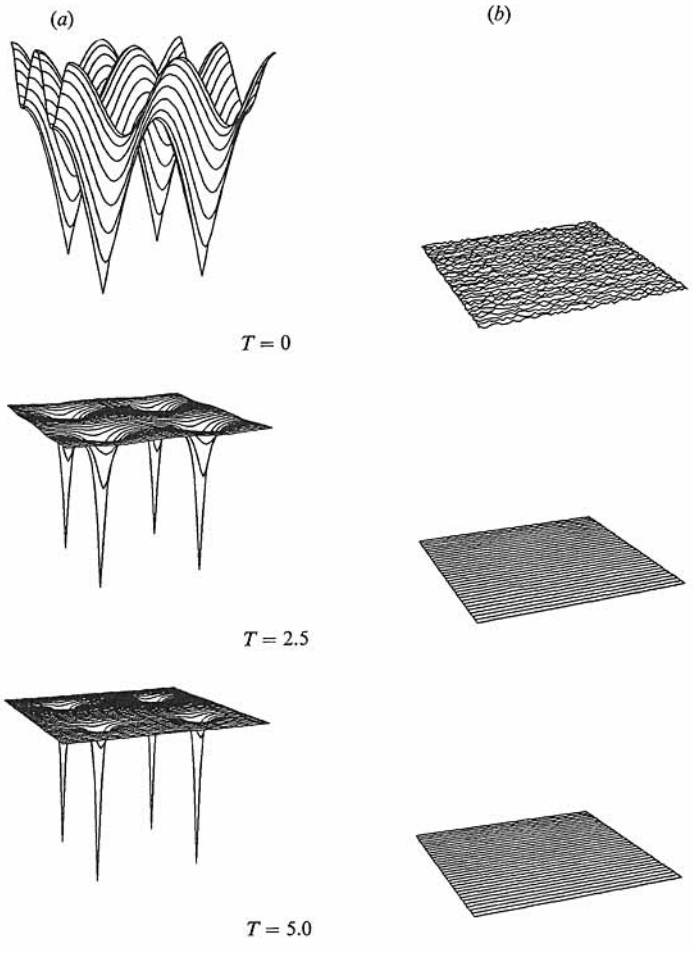

FIGURE 5. Amplitude distribution of $|A_2|$ and $|A_1|$ in the (x, z)-plane as a function of time when $\mu_1 = -0.1$, $\mu_2 = 0.6$. $a_1 = 1.0$, $a_2 = 1.2$, $b_1 = 1.6$, $b_2 = 1.5$; $\gamma_1 = 0.5$, $\gamma_2 = 0.7$, $\delta_1 = 0.25$, $\delta_2 = 0.35$; $q_x = 0.1$, $q_z = 0.1$. (*a*) Amplitude of the fundamental mode, $|A_2|$; (*b*) amplitude of the subharmonic mode, $|A_1|$.

The physical mixing layer undergoes a succession of pairing events which are responsible for the increase of shear-layer thickness with downstream distance. The equations, however, are intended to describe a single pairing sequence and the resulting increase in local thickness is not considered. The model could be expanded by adding additional subharmonic components and appropriate equations, but this was not attempted. Finally, Dallard & Browand (1993) have shown that each of these localized pairings has a finite bandwidth. That is, the transition is centred at the subharmonic wavelength, but the growing subharmonic patch contains a spread of wavelengths. The degree of tuning, or the narrowness of the wavelength band, depends greatly upon how the mixing layer is forced. These subtleties are not incorporated in the present model.

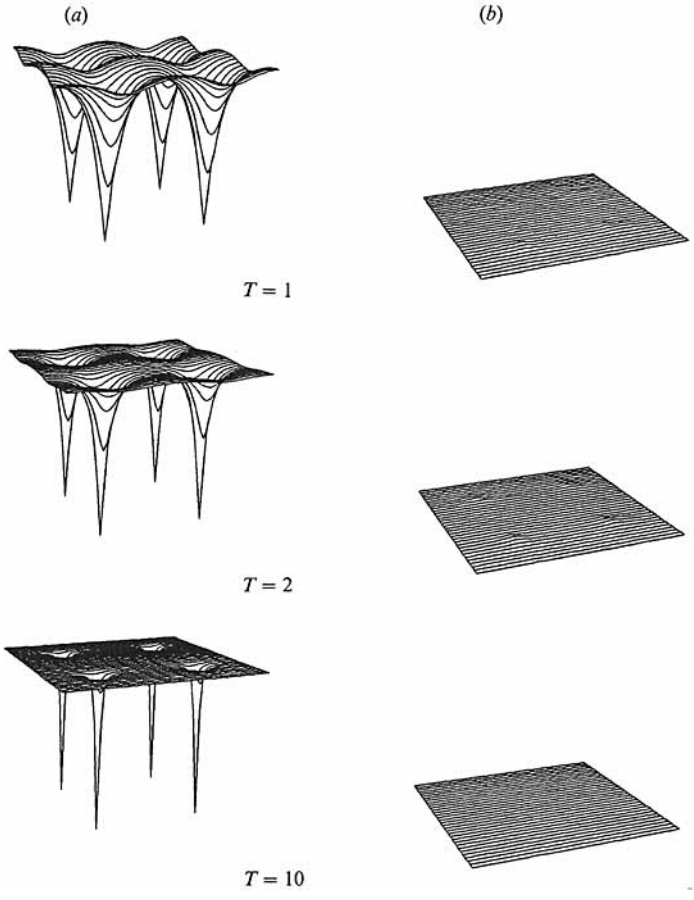

FIGURE 6. Amplitude distribution of $|A_2|$ and $|A_1|$ in the (x,z)-plane as a function of time when $\mu_1 = 0.2$. The other parameters are the same as in figure 5.

3. Numerical simulation of the pairing process: a qualitative comparison with experiments

The model equations are numerically solved in a rectangular domain $[0, 2\pi/q_x] \times [0, 2\pi/q_z]$ in the (x,z)-plane. A pseudo-spectral method is used for the spatial discretization with periodic boundary conditions in both x- and z-directions. The collocation points are uniformly distributed according to

$$x_i = \frac{2\pi i}{q_x N_x}, \quad i = 0, 1, \ldots, N_x - 1 \tag{12}$$

and

$$z_j = \frac{2\pi j}{q_z N_z}, \quad j = 0, 1, \ldots, N_z - 1 \tag{13}$$

with a total of $N_x \times N_z$ points. Initial conditions are specified by the values of A_1 and A_2 at $T = 0$. The Fourier transforms required in the spatial discretizations are performed by calling FFT routines and the time-marching procedure is a predictor-corrector algorithm based on the leap-frog scheme.

The initial conditions for most of the numerical simulations are chosen as

$$A_2 = \cos(q_x x) + \mathrm{i} \cos(q_z z), \tag{14}$$

$$A_1 = \text{white noise}. \tag{15}$$

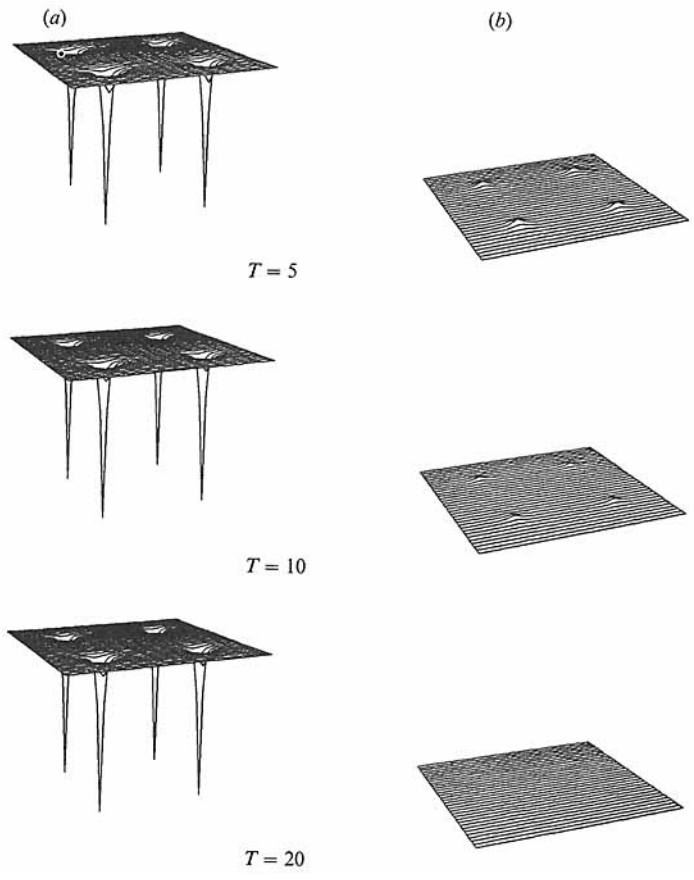

FIGURE 7. Amplitude distribution of $|A_2|$ and $|A_1|$ in the (x,z)-plane as a function of time when $\mu_1 = 0.5$. The other parameters are the same as in figure 5.

In all cases, this state quickly relaxes to a pattern composed of four dislocations located at the points $x = \pi/2q_x, 3\pi/2q_x$ and $z = \pi/2q_z, 3\pi/2q_z$, the fundamental state $|A_2| = (\mu_2/a_2)^{\frac{1}{2}}$ being attained everywhere else in the field. This initial configuration will be selected to study defect-induced pairing. The parameters in our computations are chosen to be:

$$a_1 = 1.0, \quad a_2 = 1.2; \quad b_1 = 1.6, \quad b_2 = 1.5; \quad \gamma_1 = 0.5, \quad \gamma_2 = 0.7;$$

$$\delta_1 = 0.25, \quad \delta_2 = 0.35; \quad q_x = 0.1, \quad q_z = 0.1,$$

and they satisfy the condition

$$a_1 a_2 - b_1 b_2 < 0.$$

As will be discussed in §3.4, variations in the diffusion coefficients γ_1, γ_2, δ_1 and δ_2 do not affect the major pairing process to be investigated. When $\mu_2 = 0.6$, the bifurcation points in figure 3 take the specific values $\mu_a = 0.4$ and $\mu_b = 0.8$. Four cases have been computed at the control parameter values $\mu_1 = -0.1, 0.2, 0.5$ and 0.7 respectively. These parameter settings correspond to points A, B, C and D on the bifurcation diagram of figure 3.

3.1. *The case $\mu_1 < \mu_c$: no pairing*

In order to explore the numerical results, the amplitudes $|A_1|$ and $|A_2|$ are plotted with respect to x and z at different times. In figure 5, we present the amplitude plots of the evolution for $\mu_1 = -0.1$ which corresponds to point A on the bifurcation

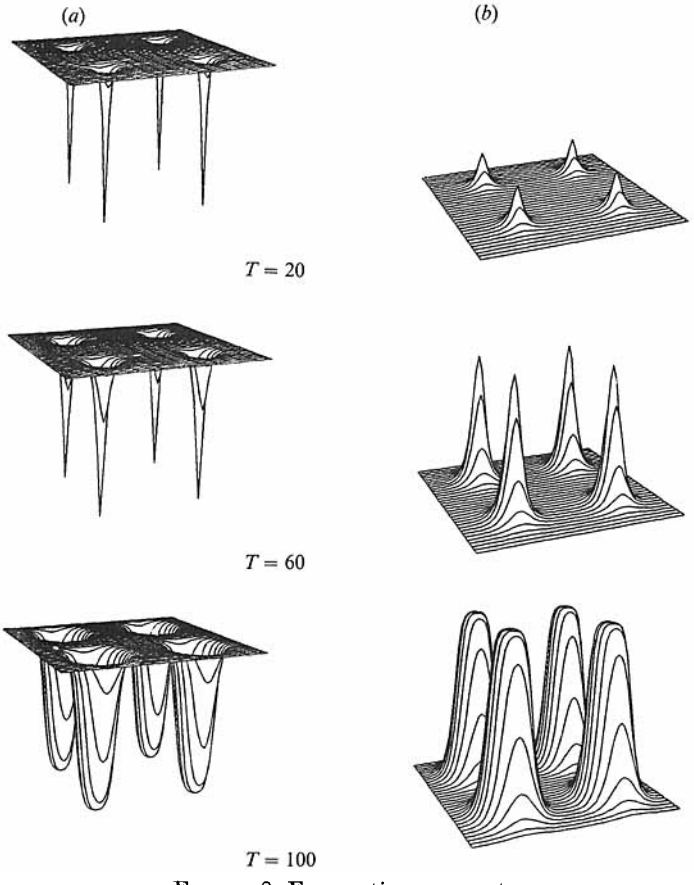

FIGURE 8. For caption see next page

diagram of figure 3. The phase portrait at this parameter value is shown in figure 4(*a*). The only stable stationary state is the fundamental solution. From the amplitude plot of figure 5, one can see that the solution quickly relaxes to the required state composed of the fundamental solution with four dislocations. The white noise perturbation has died out at $T = 5$ leaving $A_1 = 0$ everywhere. In the next computation, the control parameter is set at $\mu_1 = 0.2$ which corresponds to point B of figure 3 and to the phase portrait displayed in figure 4(*b*). There is now one more fixed point than for the case $\mu_1 = -0.1$: it represents an unstable subharmonic stationary solution. The amplitude development is plotted in figure 6. Note that the subharmonic A_1 mode grows initially at the dislocation points but it ultimately decays. The final state is again constituted of the fundamental solution with four dislocations. When the parameter is increased to $\mu_1 = 0.5$, point C of figure 3, the stationary states have reached the configuration shown in figure 4(*c*). In this case, both the fundamental solution and the subharmonic solution are stable. However, the control parameter is smaller than its critical value, $\mu_1 < \mu_c$, so that the fundamental solution is stable and the subharmonic solution is metastable as previously mentioned. One therefore cannot expect any dramatic changes to occur from the evolutions of the previous cases. The amplitude plots in figure 7 indicate that the subharmonic mode does increase in the dislocation cores over a relatively longer time than in the case $\mu_1 = 0.2$. But, ultimately the subharmonic mode decays to zero.

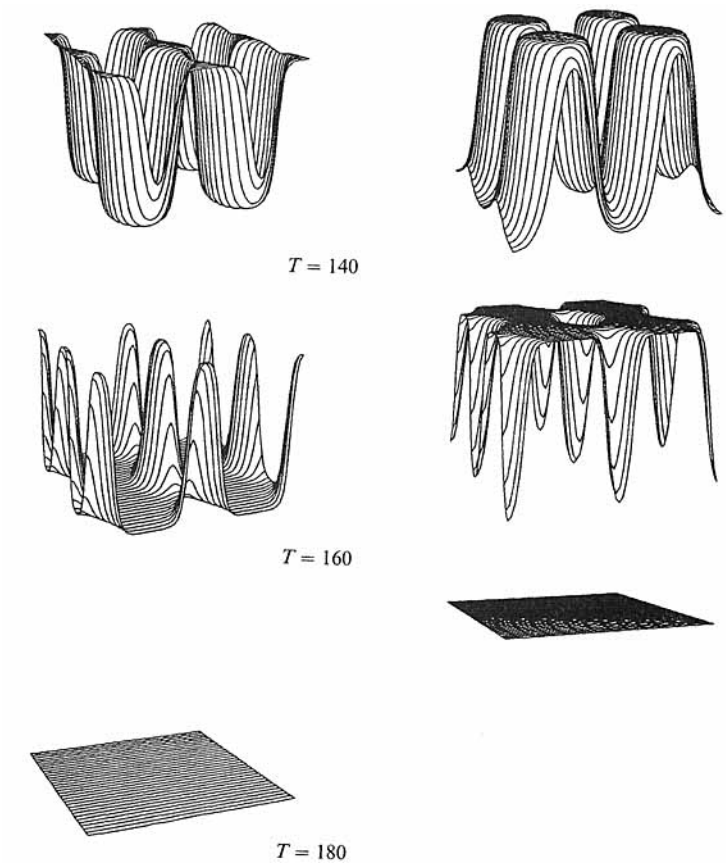

FIGURE 8. Amplitude distribution of $|A_2|$ and $|A_1|$ in the (x, z)-plane as a function of time when $\mu_1 = 0.7$. The other parameters are the same as in figure 5.

3.2. *The case $\mu_1 > \mu_c$: pairing*

When the parameter μ_1 is set to 0.7 (point D of figure 3, $\mu_1 > \mu_c$), the subharmonic solution is stable and the fundamental solution becomes metastable. The evolution for this case is illustrated in figure 8 with the same initial conditions as before. The early evolution is similar to the case $\mu_1 = 0.5$, with $|A_1|$ growing. However, the growth of $|A_1|$ here does not stop as before but instead continues as shown in figure 8. At time $T = 100$, $|A_1|$ saturates and $|A_2|$ has uniformly decayed to a flat zero level in a finite region encompassing the original dislocations. At this moment, pairing has taken place in these domains because the subharmonic mode becomes locally dominant. As time increases, the paired areas expand until, at $T = 180$, the entire computational area is fully occupied by the subharmonic solution $|A_1| = (\mu_1/a_1)^{\frac{1}{2}}$. The first-order pairing process is then completed.

In order to compare with the experimental results, we introduce the carrier waves and represent the contour lines of the perturbed vertical velocity, Re (ψ), where ψ is defined by (3) in §2.1. One plot of this kind is illustrated in figure 9(*b*). The rolls in this figure can be considered as the spanwise vortices that dominate the development of mixing layers. One can clearly see the presence of dislocations from the appearance of extra rolls locally within the domain. To focus on only one isolated dislocation, we blow up the left bottom quarter of the figure and label the resulting plot figure 9(*c*). The corresponding amplitude plot for this initial condition is given in figure 9(*a*) for

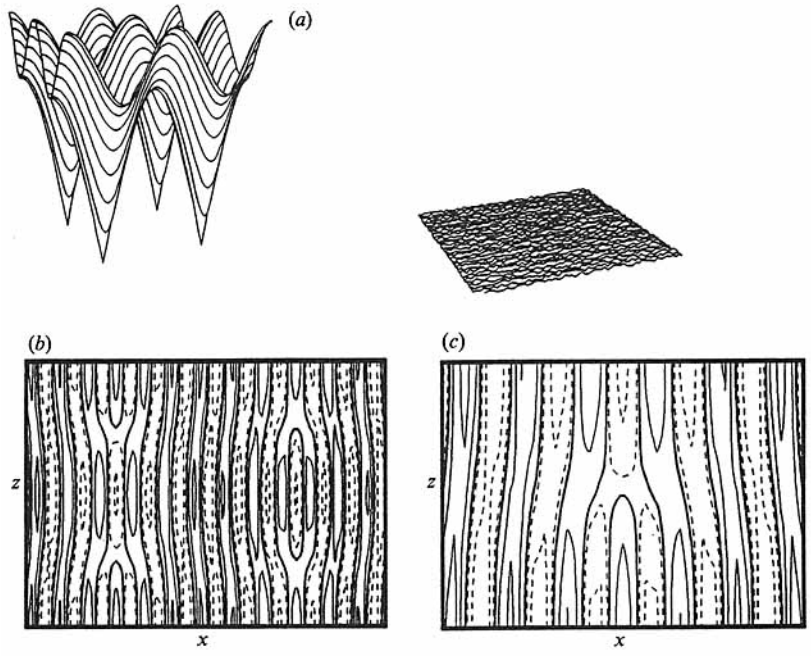

FIGURE 9. Initial amplitudes and contours of the perturbation velocity, $\mathrm{Re}(\psi)$. (*a*) Amplitude distribution of $|A_2|$ (left) and $|A_1|$; (*b*) level contours of $\mathrm{Re}(\psi)$ in the entire computational field; (*c*) blow-up of lower left quarter of (*b*). Solid and dashed lines respectively represent positive and negative values.

reference. In figure 10, contours are displayed at different times for the parameter value $\mu_1 = 0.7$. The flow near the dislocation undergoes a continuous, gradual change in shape until T reaches about 80. For $T > 80$, pairing occurs in the centre of the domain due to the appearance of structures at the subharmonic wavenumber $\frac{1}{2}\alpha$. As time increases further, the area occupied by the structures at the subharmonic wavenumber becomes larger and larger. The final state consists entirely of straight vortices of wavenumber $\frac{1}{2}\alpha$ as shown in the last plot of figure 10 at $T = 180$. No further changes take place for $T > 180$.

Corresponding experimental results in mixing layers have been obtained as shown in figure 11, which displays spatio-temporal structures at different downstream stations Rx/λ_1, where $R = \Delta U/2\bar{U}$ is the velocity ratio, x is the distance from the trailing edge of the splitter plate, and λ_1 is the initially most amplified wavelength. The dark and light regions again form a two-level contour plot of the measured streamwise perturbation velocity. The initial dislocation in the velocity field is generated by acoustically forcing the mixing layer with a slight frequency mismatch along the span (Dallard & Browand 1993). The downstream evolution provides the evidence for defect-induced pairing in the mixing layer. The field near the dislocation steepens locally as the size of the dislocation region shrinks – a behaviour mirrored by the calculations. At the station $Rx/\lambda_1 = 1.5$, two vortices at the fundamental wavenumber pinch to form a small area dominated by subharmonic structure. The region dominated by the subharmonic continues to grow in size, as does the subharmonic region in the calculations.

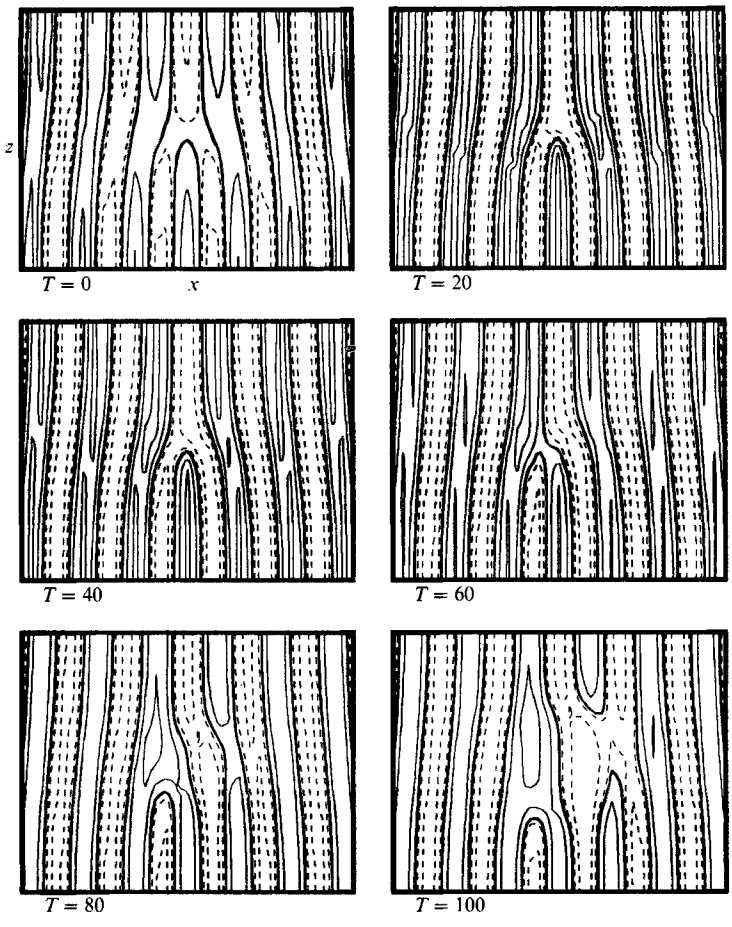

FIGURE 10. For caption see facing page.

3.3. *Pairing induced by defect-free initial conditions*

In the experimental observations, pairing may also appear in a region where the fundamental mode is weak but where a defect may not be present (Dallard & Browand 1993). In this case also, the model equations exhibit phenomena that are consistent. One example is shown in figure 12, where the initial condition is chosen as

$$A_2 = |\cos(q_x x)| + \mathrm{i}\,|\cos(q_z z)|, \qquad A_1 = \text{white noise}, \tag{16}$$

and the computational domain is of size $\pi/q_x \times \pi/q_z$ with only one point where $A_2 = 0$. In contrast to the previous case, both parts of A_2 in (16) are positive, there is no phase jump, and therefore no defects are generated. The evolution of this defect-free state shown in figure 12 indicates that the fundamental mode A_2 increase everywhere initially when the level of the white-noise perturbation of the subharmonic mode A_1 is low. In spite of this, at the centre point where $|A_2|$ is smallest, $|A_1|$ grows gradually. At around $T = 6$ (not shown), the growth of $|A_2|$ at the centre point cannot proceed but instead $|A_2|$ begins to decay, while $|A_1|$ continues to increase locally. Saturation takes place as shown in the amplitude plot at about $T = 50$, and the remaining evolution is the same as the case with dislocations – namely the area dominated by the subharmonic expands. The final state is $A_2 = 0$ and $|A_1| = (\mu_1/a_1)^{\frac{1}{2}}$, the uniform

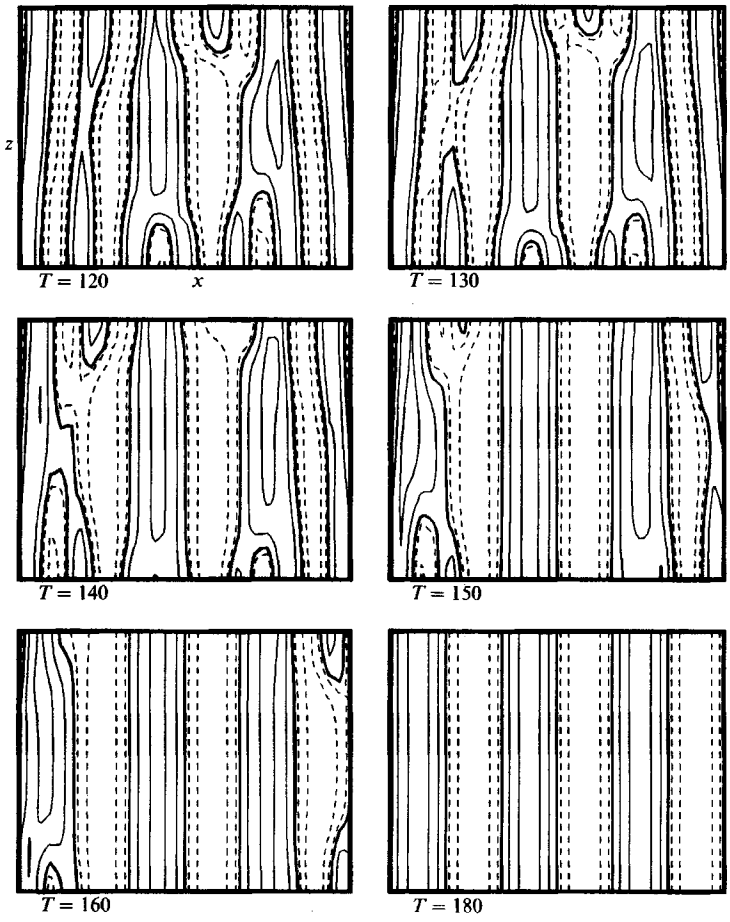

FIGURE 10. Dislocation-induced pairing process when the subharmonic solution is stable for $\mu_1 = 0.7$. The other parameters are the same as in figure 5. Level contours of Re (ψ) are shown in each frame with increasing time.

subharmonic solution. Thus, the presence of defects is not necessary to promote a three-dimensional subharmonic transition. A localized region, where the fundamental has a low amplitude, is sufficient.

3.4. *Response to changes in model coefficients*

When the diffusion coefficients $\gamma_1,\gamma_2,\delta_1$, and δ_2 are changed, the basic pairing process remains unaffected but the geometry of the expanding area dominated by the subharmonic may change. Contour plots of $|A_1|$ and $|A_2|$ indicate that the cross-sections are ellipses depending mainly on the ratio of γ_1/γ_2. The major axes of the ellipses coincide with the directions of larger diffusion coefficient in (1). The ratio δ_1/δ_2 plays the same role but it is effective only when γ_1/γ_2 is close to one.

The behaviour of the solutions near the critical parameter μ_c is not entirely clear. This is because this critical value is defined with respect to the stable or metastable nature of homogeneous solutions only. A stability analysis of stationary states with defects could be helpful in obtaining a more detailed understanding of the result. What has been confirmed in the numerical simulations is that there does exist a critical spatial state for each control parameter value μ_1 in the range $\mu_a < \mu_1 < \mu_b$. This

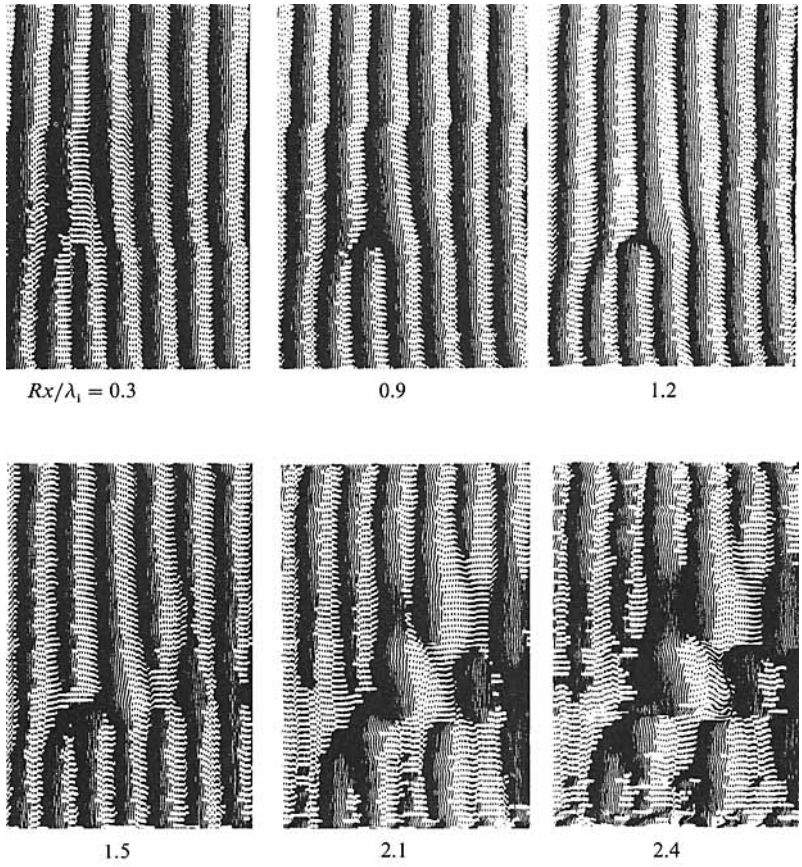

FIGURE 11. Experimental results illustrating pairing in the vicinity of a dislocation defect generated in the mixing layer. The flow is weakly forced. Solid lines and dashed lines represent positive and negative streamwise fluctuation velocities respectively. Each frame pertains to a specific value of normalized streamwise distance Rx/λ_1.

state is unstable and behaves as a critical size for a 'bubble' containing the subharmonic. When an initial state corresponds to a uniform fundamental plus a 'bubble' of subharmonic larger than the critical size, the 'bubble' will continually increase in size. On the other hand, if the initial 'bubble' size is smaller than the critical size, the 'bubble' will shrink and eventually disappear.

4. Growth in the number of defects: a quantitative comparison with experiments

From the constant $\mathrm{Re}(\psi)$ contours of figure 10, one can clearly detect the original defect by the extra vortex in the pattern. Once pairing takes place the original defect disappears, yet phase lines break and reconnect so as to produce a number of defects lying along the boundary of the expanding regions. Their number can be counted and compared with experimental observations as a quantitative measure of comparison. It is first necessary to tune the diffusion coefficients in the model by matching with experiment the rate of spread of the growing subharmonic region.

Dallard & Browand (1993) have measured the rates of spread in x and z of the

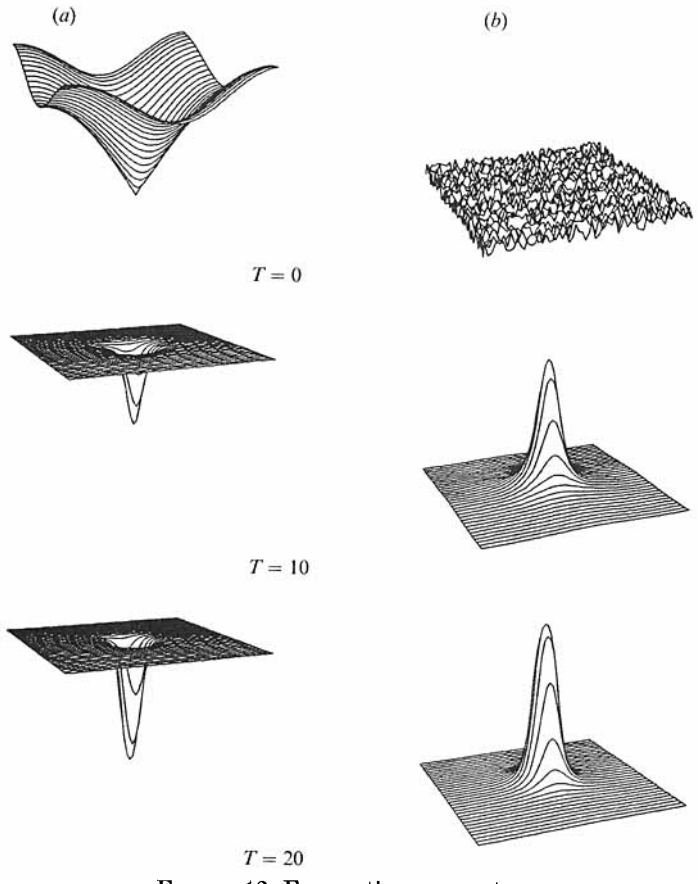

FIGURE 12. For caption see next page

subharmonic region. Since the time and space scales of the model have not been scaled to fit the real physical situation, the comparison of the velocities themselves is meaningless. The useful quantity is the ratio of the expansion velocity in the streamwise direction to that in the spanwise direction. It is this ratio which influences the number of defects. The ratio of velocities, $r = V_z/V_x$, found from experiments is about $r = 1.5 \pm 0.1$ (Dallard & Browand 1993). The same ratio is obtained for the model as follows. Notice that only the diffusion terms contain x or z dependence. The terms

$$\gamma_1 \partial^2/\partial x^2 + \gamma_2 \partial^2/\partial z^2$$

can be transformed to

$$\partial^2/\partial x'^2 + \partial^2/\partial z'^2$$

by use of the transformation $x = \gamma_1^{\frac{1}{2}} x'$ and $z = \gamma_2^{\frac{1}{2}} z'$.

In the coordinate system x', z', the spreading domain of subharmonic dominance must be circular. It follows that setting $r = (\gamma_2/\gamma_1)^{\frac{1}{2}}$ will give the appropriate spreading rate for the model. For the calculation, the diffusion coefficients are taken to be $\gamma_1 = 0.5$, $\gamma_2 = 0.5 \times (1.5)^2 = 1.125$. Finally, it is not unreasonable to choose the diffusion coefficients in the equation for the fundamental to have the same ratio. That is, we take $\delta_1 = \gamma_1, \delta_2 = \gamma_2$. All other constants are kept at the previous values, with $\mu_1 = 0.7$. For these settings, the pairing is qualitatively similar to that shown in figure 8.

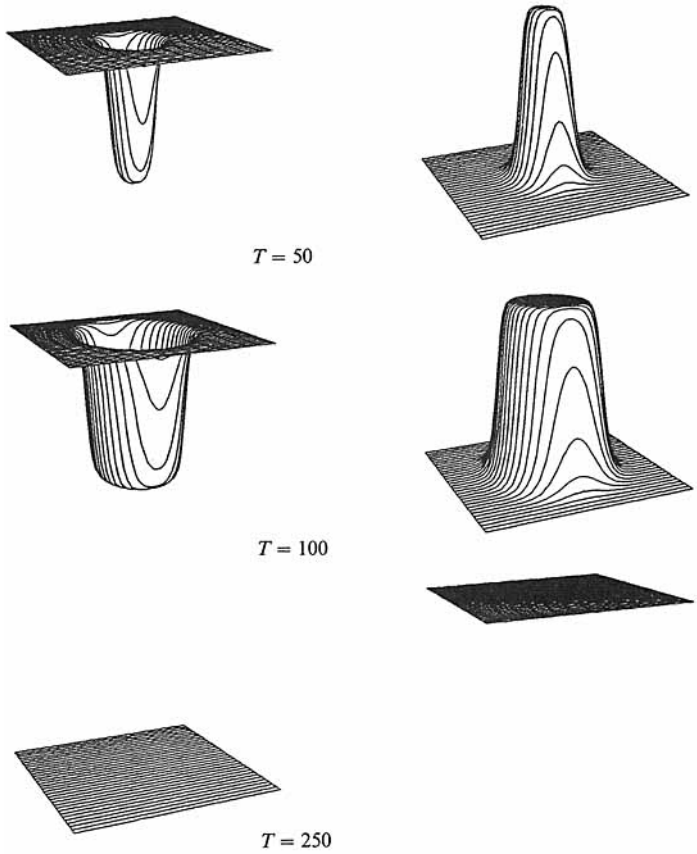

FIGURE 12. Amplitude distribution of $|A_2|$ and $|A_1|$ in the (x, z)-plane as a function of time for $\mu_1 = 0.7$ with defect-free initial conditions. The other parameters are the same as in figure 5.

Following Dallard & Browand (1993), define the x, z centre of the expanding region of subharmonic dominance as

$$x_c = \frac{1}{Q}\sum_i \sum_j x_i |A_1|^2_{i,j}, \tag{17}$$

$$z_c = \frac{1}{Q}\sum_i \sum_j z_j |A_1|^2_{i,j}, \tag{18}$$

and use the second moment about the centre

$$x_\sigma = \left(\frac{1}{Q}\sum_i \sum_j (x_i - x_c)^2 |A_1|^2_{i,j}\right)^{\frac{1}{2}}, \tag{19}$$

$$z_\sigma = \left(\frac{1}{Q}\sum_i \sum_j (z_j - z_c)^2 |A_1|^2_{i,j}\right)^{\frac{1}{2}}, \tag{20}$$

as a measure of the planform boundaries. Here

$$Q = \sum_i \sum_j |A_1|^2_{i,j} \tag{21}$$

and the $|A_1|^2_{i,j}$ are the local values of $|A_1|^2$ which are larger than a threshold value

$$A_s^2 = s|A_1|^2_{\max} = s a_1/\mu_1,$$

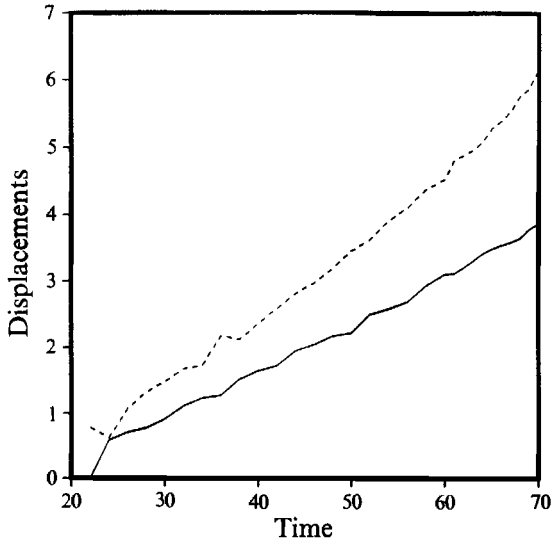

FIGURE 13. Variations with time of x_σ (——) and z_σ (– – – –) defined by (19) and (20) in the text. Parameters settings are: $\mu_1 = 0.7$, $\mu_2 = 0.6$; $a_1 = 1.0$, $a_2 = 1.2$, $b_1 = 1.6$, $b_2 = 1.5$; $\gamma_1 = 0.5$, $\gamma_2 = 1.125$. $\delta_1 = 0.5$, $\delta_2 = 1.125$.

with s being chosen as a factor less than one. The indices i and j are summed over one quarter of the computational domain, since only one defect is produced experimentally. The variations of x_σ and z_σ for $s = 0.5$ are displayed in figure 13. Though the values of V_x and V_z calculated through the slopes of displacement-time lines depend on the threshold value s, the velocity ratio r is independent of this threshold, as is approximately true for the experiment. Our anticipated value is 1.5 as discussed above. The measured value from the numerical result is about $r = 1.57$, and this is deemed close enough for comparison of the number of defects.

The initial surface density of defects counted near the origin of the mixing layer is approximately $1\text{–}2 \times 10^{-2}$, where the unit of area is taken to be $\lambda \times \lambda$ (actually $\lambda \times \lambda/\bar{U}$ in the experiment of Browand & Prost-Domasky 1991). Thus 1–2 defects would initially be found – on average – in an area of width 10λ and length 10λ (or time interval $10\lambda/\bar{U}$). The corresponding calculation initially places one defect in an area $10\lambda \times 10\lambda$. The sequence is illustrated in figure 14 as a function of time. The largest number of defects spawned in the calculation domain is five. Thus the ratio of increase in number is 5:1. In the experiment, the average initial density is taken to be 1.5×10^{-2}, and the real maximum density is measured to be about 10^{-1}. The ratio of increase in number is effectively about 7:1, close to the number estimated. This is taken to be additional verification of the ability of the model to predict the complex geometric properties of growing turbulent mixing layer.

5. Concluding remarks

The model of defect-induced pairing successfully describes how the subharmonic component is preferentially generated in the core regions of structural defects in the initial vortex pattern. Success is measured qualitatively by the correspondence of the pattern with the experimental results. There is quantitative agreement expressed by the correspondence in the number of new defects created during such a localized pairing process. The present description is somewhat different from the conventional

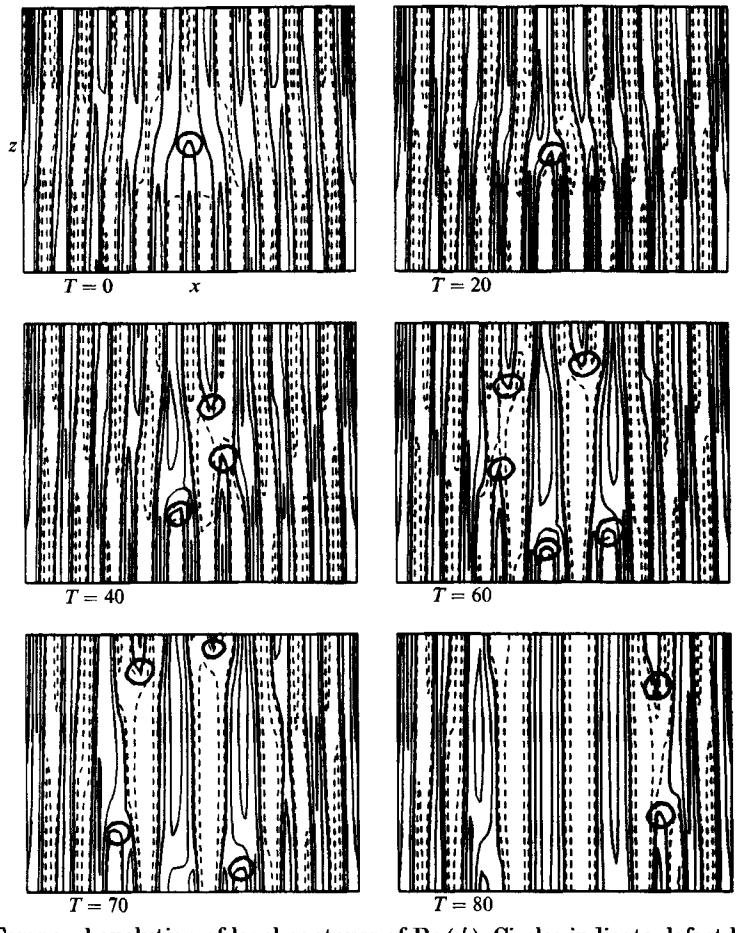

FIGURE 14. Temporal evolution of level contours of Re (ψ). Circles indicate defect locations. Note that additional defects are spawned during pairing process. Parameters settings are the same as in figure 13.

manner of describing flows transitioning to turbulence. As mentioned in the introduction, similar evolution equation models have been used successfully to describe evolution in Rayleigh–Bénard convection, binary convection, and other closed flow systems. They have not been widely applied to the study of parallel shear flows. As used here, the model equations qualitatively describe the evolution of the large-scale structures in the shear flow. Unique values for the coefficients of the various terms have not been obtained from available experimental data. However, we have demonstrated that such a model can serve to describe interesting and complex physics.

The authors have benefitted from many stimulating discussions with L. G. Redekopp. This research is supported by the Office of Naval Research, under contracts # N0001486-K-0679 and N00014-89-J-1400, by ATT through the Affiliates Research Program with USC, and by a travel grant from NATO. Part of the computer time was provided by San Diego Supercomputer Center.

REFERENCES

BALIAN, R., KLEMANN, M. & POIRIER, J. 1981 *Physics of Defects*. Elsevier North-Holland.

BROWAND, F. K. & PROST-DOMASKY, S. 1990 Experiment on pattern evolution in the 2-d mixing layer. In *New Trends in Nonlinear Dynamics and Patterning Phenomena: The Geometry of Nonequilibrium* (ed. P. Coullet & P. Huerre). NATO ASI Series B, pp. 159–169. Plenum.

BROWAND, F. K. & TROUTT, T. R. 1980 A note on spanwise structure in the two-dimensional mixing layer. *J. Fluid Mech.* **97**, 771–781.

BROWAND, F. K. & TROUTT, T. R. 1985 The turbulent mixing layer: geometry of large vortices. *J. Fluid Mech.* **158**, 489–509.

BROWN, G. L. & ROSHKO, A. 1974 On density effects and large structure in turbulent mixing layers. *J. Fluid Mech.* **64**, 775–816.

CHOMAZ, J. M., HUERRE, P. & REDEKOPP, L. G. 1988 Bifurcations to local and global modes in spatial-developing flows. *Phys. Rev. Lett.* **60**, 25–28.

CHURILOV, S. M. & SHUKHMAN, I. G. 1987 Note on weakly nonlinear stability theory of a free mixing layer. *Proc. R. Soc. Lond.* A **409**, 351–367.

COULLET, P., GIL, L. & REPAUX, D. 1989 Defects and subcritical bifurcations. *Phys. Rev. Lett.* **62**, 2957–2960.

CROSS, M. C. 1988 Structure of nonlinear traveling-wave states in finite geometries. *Phys. Rev.* A **38**, 3593–3600.

DALLARD, T. & BROWAND, F. K. 1993 The growth of large scales at defect sites in the plane mixing layer. *J. Fluid Mech.* **247**, 339–368.

HO, C. M. & HUANG, L. S. 1982 Subharmonics and vortex merging in mixing layers. *J. Fluid Mech.* **119**, 443–473.

HO, C. M. & HUERRE, P. 1984 Perturbed free shear layers. *Ann. Rev. Fluid Mech.* **16**, 365–424.

HUERRE, P. 1987 On the Landau constant in mixing layers. *Proc. R. Soc. Lond.* A **409**, 369–381.

KELLY, R. E. 1967 On the stability of an inviscid shear layer which is periodic in space and time. *J. Fluid Mech.* **27**, 657–689.

KELLY, R. E. 1968 On the resonant interaction of neutral disturbances in two inviscid shear flows. *J. Fluid Mech.* **31**, 789–799.

LIFSHITS, E. M. & PITAEVSKII, L. P. 1981 *Physical Kinetics*. Pergamon.

MICHALKE, A. 1964 On the inviscid instability of the hyperbolic tangent velocity profile. *J. Fluid Mech.* **19**, 543–556.

MONKEWITZ, P. A. 1988 Subharmonic resonance, pairing and shedding in the mixing layer. *J. Fluid Mech.* **188**, 223–252.

WINANT, C. D. & BROWAND, F. K. 1974 Vortex pairing: the mechanism of turbulent mixing-layer growth at moderate Reynolds number. *J. Fluid Mech.* **63**, 237–255.